


<https://doi.org/10.1038/s41612-025-01037-5>

# Unstable permafrost regions experience more severe heatwaves in a warming climate

Xiangfei Li<sup>1</sup>, Lin Zhao<sup>1</sup> , Shuo Wang<sup>2</sup>, Xinghua Cheng<sup>3</sup> & Lingxiao Wang<sup>1</sup>

Heatwaves are causing catastrophic consequences on natural and socioeconomic systems yet they remain under-investigated in permafrost regions. Using simulations from the Coupled Model Intercomparison Project Phase 6 (CMIP6), we present a comprehensive assessment of recent and future heatwaves across the permafrost regions of the Northern Hemisphere (PRNH). Our focus is on the characteristics of summer and winter heatwaves as well as their potential implications for infrastructure stability. Results show that the PRNH has experienced increasing heatwaves over the past decades and is projected to face more frequent and intense heatwaves, especially under higher warming levels. Globally, summer heatwaves occur more frequently, whereas winter heatwaves exhibit higher intensity, with distinct regional behaviors. Both summer and winter heatwaves in the Arctic and the Qinghai-Tibetan Plateau (QTP) occur more frequently than that in mid-latitude regions. The mid-latitudes present the strongest summer heatwaves, while the Arctic endures the most severe winter heatwaves. Historically, the Arctic and the QTP have been more affected by winter heatwaves due to their longer heatwave days and stronger intensity compared to summer heatwaves. Under warming scenarios, the Arctic is projected to continue facing greater winter heatwave pressure on account of the quick-enhancing intensity. Conversely, the QTP will be more affected by summer heatwaves due to their longer and rapidly growing heatwave days. Further analyses indicate that permafrost regions with high geohazard potential (GP) will come under greater summer heatwave stress, particularly in the Arctic and QTP, associated with longer heatwave days. The high-GP regions in Eurasia, however, are expected to bear more severe winter heatwaves driven by higher intensity. These findings deepen our understandings of heatwaves in PRNH and highlights the potential impacts of heatwaves on geohazards in permafrost regions.

Permafrost is soil and rocks below the Earth's surface whose temperature is less than 0 °C for at least two consecutive years, which covers ~20% of land area of the Northern Hemisphere (Fig. 1a)<sup>1</sup>. In the context of climate warming, permafrost is experiencing significant degradation over the past decades, resulting in soil warming<sup>2</sup>, active layer thickening<sup>3</sup>, shrinkage of permafrost extent<sup>4</sup>, and formation of various thermokarst landforms<sup>5,6</sup>. Permafrost areas are featured with year-round freeze-thaw cycles<sup>7</sup>, abundant ground ice<sup>8</sup>, and giant soil organic carbon<sup>9</sup>, whose disturbances not only profoundly affect local hydro-eco-geomorphology processes<sup>10,11</sup> and infrastructures<sup>12</sup>, but also change the climate dynamics and global carbon cycles<sup>13</sup>.

Heatwaves is a period of abnormally high temperatures lasting several days<sup>14</sup>, which is extensively reported and exerting important implications across permafrost regions<sup>15–18</sup>. In summer with abnormally high temperatures, the permafrost area generally shows higher temperature and deeper active layers<sup>19</sup>. And such thermal response maybe detectable at deep layers and last for years<sup>20,21</sup>. In situ observations indicated that the 2003 heatwave across the Europe has deepen the active layer in the year, and since then caused long-term degradation of permafrost in the Swiss Alps<sup>22</sup>. Studies in the permafrost regions of Tanggula on the Qinghai-Tibetan Plateau (QTP) indicated a positive relationship between soil temperature and the duration

<sup>1</sup>School of Geographical Sciences, Nanjing University of Information Science & Technology, Nanjing, China. <sup>2</sup>Department of Land Surveying and Geo-Informatics, Research Institute for Land and Space, The Hong Kong Polytechnic University, Hong Kong, China. <sup>3</sup>Department of Natural Resources and the Environment, University of Connecticut, Storrs, CT, 06269, USA. ✉e-mail: [lzhao@nuist.edu.cn](mailto:lzhao@nuist.edu.cn)

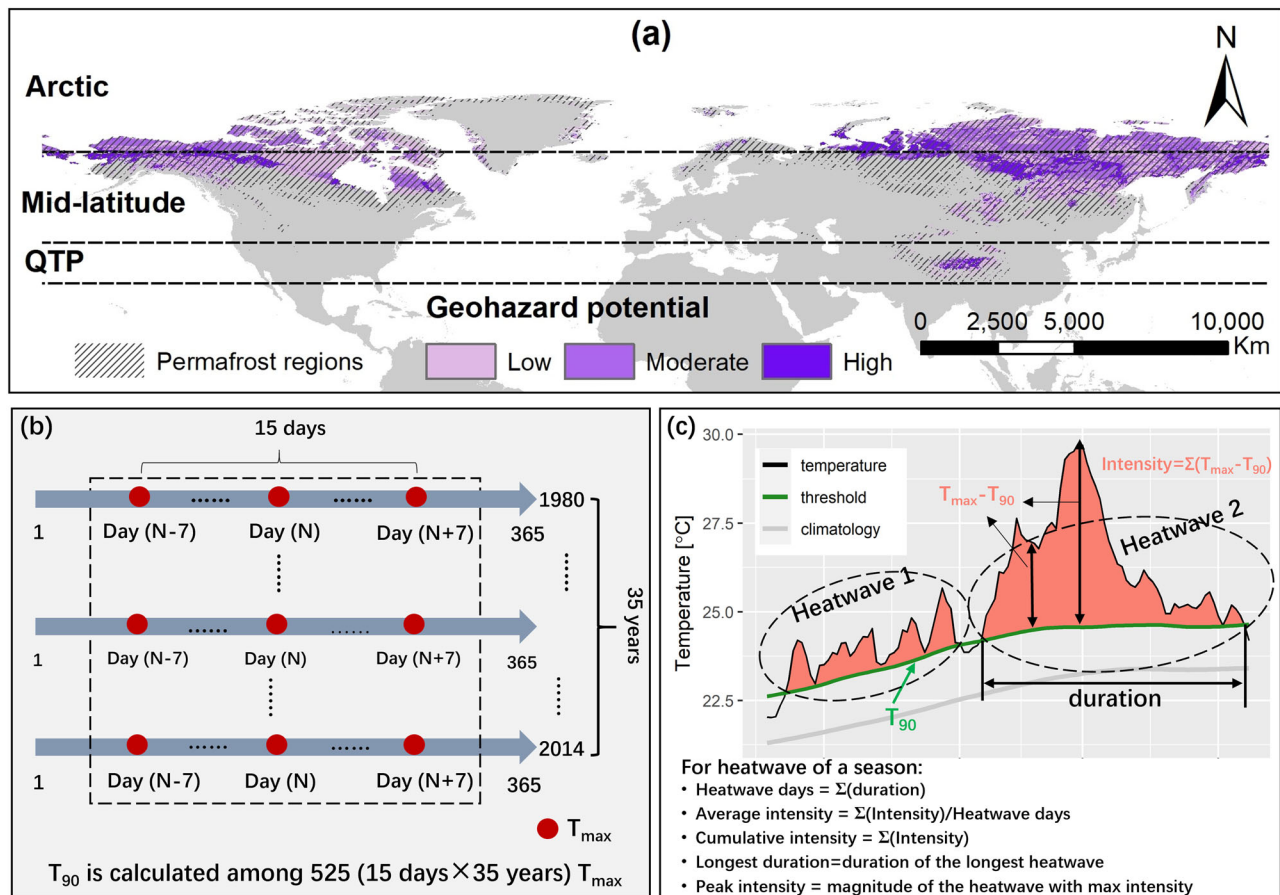


**Fig. 1 | Study area and the conceptual diagram of heatwave identification.** The hatching indicates the permafrost region over the Northern Hemisphere (a), which is divided into three parts by dashed lines: the Arctic, the Mid-latitude, and the

Qinghai-Tibetan Plateau (QTP). Geohazard potential displayed here is the projected result for the middle of the century (2041–2060) under the RCP 8.5 scenario<sup>110</sup>. The conceptual diagram of the determination of  $T_{90}$  (b) and heatwave metrics (c).

and intensity of heatwaves, and heatwaves explained ~13% of seasonally thawing depth<sup>23,24</sup>. Heatwaves, superimposed on a warming trend, are also likely to cause hazardous irregular acceleration in permafrost thawing by heating soil temperature rapidly and melting ground ice in a very short period<sup>20</sup>. This favors a variety of abrupt thaw events in ice-rich areas, such as ground collapse, detachment slides, retrogressive thaw slumps and rockfalls<sup>25–28</sup>, leading to the further exposure and degradation of deep permafrost<sup>29,30</sup>. When the permafrost thaw abruptly, substantial amounts of carbon stored frozen in soils are emitted to the atmosphere quickly<sup>31</sup>. For example, the atmospheric concentration of methane in northern Siberia increased remarkably since June during the 2020 heatwave and remain elevated until the spring of 2021 in spite of the following low temperature and snowfall<sup>32</sup>. The carbon emissions from permafrost in turn are expected to amplify the rate of climate change and thus the degradation of permafrost<sup>31,33</sup>.

Despite the significant influence of heatwaves on permafrost, a comprehensive understanding of heatwaves in permafrost regions is still lacking. One reason is the limited sampling of heatwaves in these areas due to the sparse and uneven observations, as well as the rarity of such events by its definition<sup>34,35</sup>. Consequently, large uncertainties persist in our current knowledge of heatwaves. Additionally, given the faster warming rates during winter in cold regions<sup>36,37</sup>, winter heatwaves are increasingly reported<sup>38–40</sup>. However, few studies have focused on winter heatwaves, which is also of great impacts on permafrost<sup>41,42</sup>. Furthermore, extreme climate and weather events often have greater impacts on environmental and human systems than climate averages<sup>43</sup>, little is known about the role of heatwaves on the stability of permafrost and infrastructure.

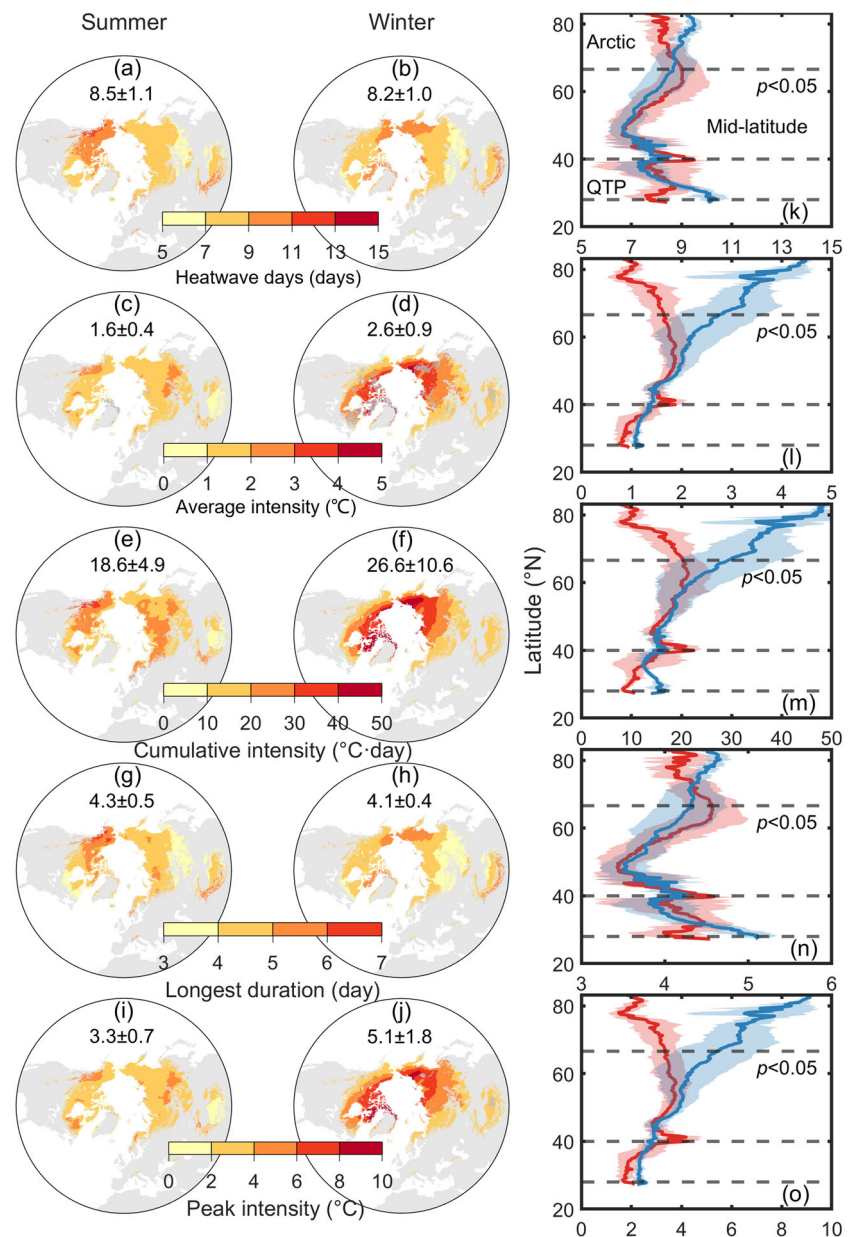
To address these research gaps, this study conducts an in-depth assessment of recent and future hotspots and the evolutionary processes of heatwaves during both summer and winter across the permafrost regions of the Northern Hemisphere (PRNH), using downscaled and bias-corrected CMIP6 data. Further analyses are conducted in regions with varying geohazard potentials (GPs, Fig. 1a) to reveal the possible implications of heatwave on infrastructure stability. The research outcomes are expected to shed light on a better understanding of heatwaves in PRNH and provide scientific guidance for preparedness, mitigation, and adaptation to such devastating heatwave pressures.

## Results

### Heatwaves in the recent climate

Figure 2 depicts the spatial patterns and temporal variations of heatwave metrics from 1980 to 2014. Permafrost regions in high-latitudes and high-altitudes (e.g., Alaska, western Canada, southern QTP and far eastern Siberia) were generally hit by more heatwaves in the past decades, with the average heatwave days ranging from 9 to 15 days per year (Fig. 2a, b, k). Moreover, winter heatwaves occurred more often than summer heatwaves in high-latitude and high-altitude regions (Fig. 2k). For average intensity, the summer heatwaves were more severe in the mid-latitudes, while winter heatwave magnitude dropped sharply with latitude. The winter average intensity was significantly higher than that of summer heatwave, with global averages of  $2.6 \pm 0.9$  vs.  $1.6 \pm 0.4$  °C, especially in the Arctic (Fig. 2c, d, l). Consequently, the spatial and latitudinal patterns of heatwave cumulative intensity generally followed those of average intensity, indicating the important role of heatwave intensity on the total heatwave pressure (Fig. 2e, f, m). In addition, PRNH tended to bear more pressure from winter

**Fig. 2 | Spatial patterns of multi-year mean heatwave metrics from 1980 to 2014.** The spatial distributions of **a, b** heatwave days (days), **c, d** average intensity ( $^{\circ}\text{C}$ ), **e, f** heatwave cumulative intensity ( $^{\circ}\text{C day}$ ), **g, h** the longest duration (day), **i, j** the peak intensity ( $^{\circ}\text{C}$ ), and **k–o** the corresponding latitudinal distributions. All grid cells in **a–j** increased significantly with  $p < 0.05$  except those dotted with gray dots, and the values represent the global averages of heatwave metrics (Mean  $\pm$  SD) during the summer (red) and winter (blue) seasons. The significance of the difference between summer and winter are indicated by the  $p$ -value.



heatwaves than summer heatwaves ( $26.6 \pm 10.6$  vs.  $18.6 \pm 4.9$   $^{\circ}\text{C day}$ ), which is more apparent in the Arctic and southern QTP (Fig. 2m). The longest duration and peak intensity of extreme heatwaves were spatially consistent with heatwave days and average intensity, respectively (Fig. 2a–d, k, l, g–j, n, o).

The PRNH has experienced an overall aggravation of heatwaves, although the trend magnitude varies across seasons, regions, and metrics (Fig. 3). In general, summer heatwave metrics increased faster than that of winter heatwaves (Fig. 3a, e, i, m, q), which is more remarkable for heatwave days and the longest duration (Fig. 3a–d, m–p). The increase slopes of heatwave days were faster than that of the longest duration. Furthermore, the growth rates of heatwave days and longest duration decreased with latitude, while the winter longest duration did the opposite (Fig. 3b–d, n–p). Although 18% of the grid boxes were detected as having non-significant trends (e.g., those in the Canadian Arctic Archipelago, eastern Siberia, and Central QTP, Fig. 2d), winter average intensity showed a positive trend across regions (Fig. 3e–h). As to the peak intensity, the percentage of non-significant grid boxes reduced dramatically (Fig. 2j), leading to a 2–3 times faster rate of increase than the average intensity (Fig. 3q–t). The regional

difference in trends in average and peak intensity were in accord with their latitudinal distributions, i.e., faster in mid-latitudes for summer heatwaves and declining with latitude for winter heatwaves (Fig. 2l, o), which was also followed by heatwave cumulative intensity (Fig. 3i–l).

### Future projection of heatwave characteristics

**Spatial patterns of future heatwaves.** Figures 4 and 5 depict the spatial and latitudinal distributions of future heatwave days, average intensity and cumulative intensity over the PRNH across four global warming levels under SSP126, SSP245, SSP370, and SSP585 scenarios, respectively. As expected, heatwave metrics for both summer and winter seasons are projected to increase with global warming levels (Fig. 4). For example, the global heatwave days (average intensity) of summer heatwave under SSP585 scenario is expected to soar to a level about 1.9 (1.3) times higher than that under SSP126 scenario, leading to approximately 2.6-fold increase in the cumulative intensity (Fig. 4a, d, i, l, q, t). Overall, the heatwaves during summer are significantly longer than winter under the four scenarios (Fig. 4a–h). The winter heatwaves, however, are expected to see higher average intensity than summer heatwaves (Fig. 4i–p). In



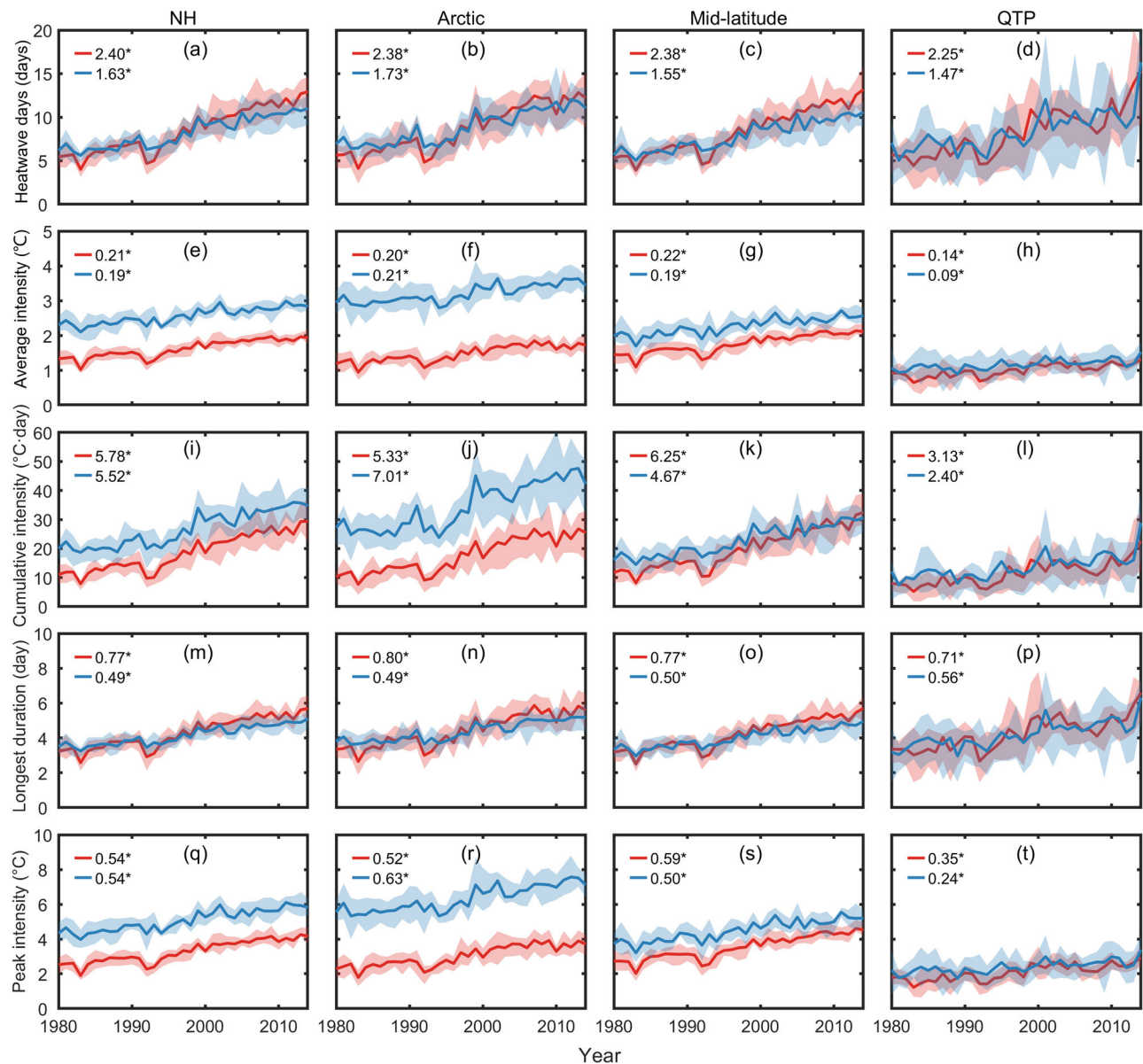


**Fig. 3 | Temporal evolution of heatwave metrics from 1980 to 2014.** The variations of **a–d** heatwave days (days), **e–h** average intensity (°C), **i–l** heatwave cumulative intensity (°C day), **m–p** the longest duration (day), and **q–t** the peak intensity (°C) over the Northern Hemisphere, the Arctic, the mid-latitude, and the Qinghai-

Tibetan Plateau (QTP). The values represent decadal trends in summer (red) and winter (blue) heatwave metrics. Asterisks represent that the trend is statistically significant ( $p < 0.05$ ). The shaded areas denote the interquartile range of heatwave metrics.

particular, the heatwave intensities of winter season in the Arctic are much more severe than those during the summer season (Fig. 5e–h). As a result, the heatwave cumulative intensities during the two seasons show a small difference globally (Fig. 4q–x), while the cumulative intensities during winter in Arctic are much greater than those during summer (Fig. 5i–l).

Consistent with the historical heatwaves, the future heatwave metrics are distinctly latitude- and altitude-dependent (Fig. 5). Heatwave days during both summer and winter in the Arctic and the QTP are longer than those in the mid-latitude. Moreover, the QTP tends to exhibit longer heatwave days compared with the Arctic, which is more apparent at high warming levels (Fig. 5a–d). Nevertheless, contrary to heatwave days, summer heatwave intensities in mid-latitudes are generally higher than those in the Arctic and the QTP (Fig. 5e–h). The winter average intensity, however, shows a strong decline with latitude (Fig. 5e–h). Consequently, the cumulative intensities of summer heatwave vary relatively small with latitude with a slight peak on the QTP. The latitudinal distribution of winter cumulative

intensity basically follows the pattern of winter heatwave days (i.e., lower in mid-latitudes while higher in the Arctic and QTP), with much higher values in the Arctic than the QTP due to the higher average intensity in the Arctic (Fig. 5i–l). The results indicate that the heatwave days and average intensity of summer heatwaves play complementary roles in contributing the cumulative intensity of summer heatwaves. In contrast, the winter heatwave cumulative intensity is mainly driven by average intensity in higher latitudes while by heatwave days in lower latitudes.

The spatial and latitudinal patterns of longest duration and peak intensity generally follow those of heatwave days and average intensity, respectively (Figs. 3, 4 S2, S3). The longest duration and peak intensity generally increase with warming levels. Additionally, summer heatwaves tend to exhibit a larger longest duration but weaker peak intensity compared to winter heatwave (Supplementary Fig. 3). Consistent with heatwave days (Fig. 5a–d), the longest duration in the mid-latitudes is shorter than that in the Arctic and QTP (Fig. 5a–d). Nevertheless, the Arctic and QTP share approximately similar longest durations (Supplementary Fig. 4a–d), which

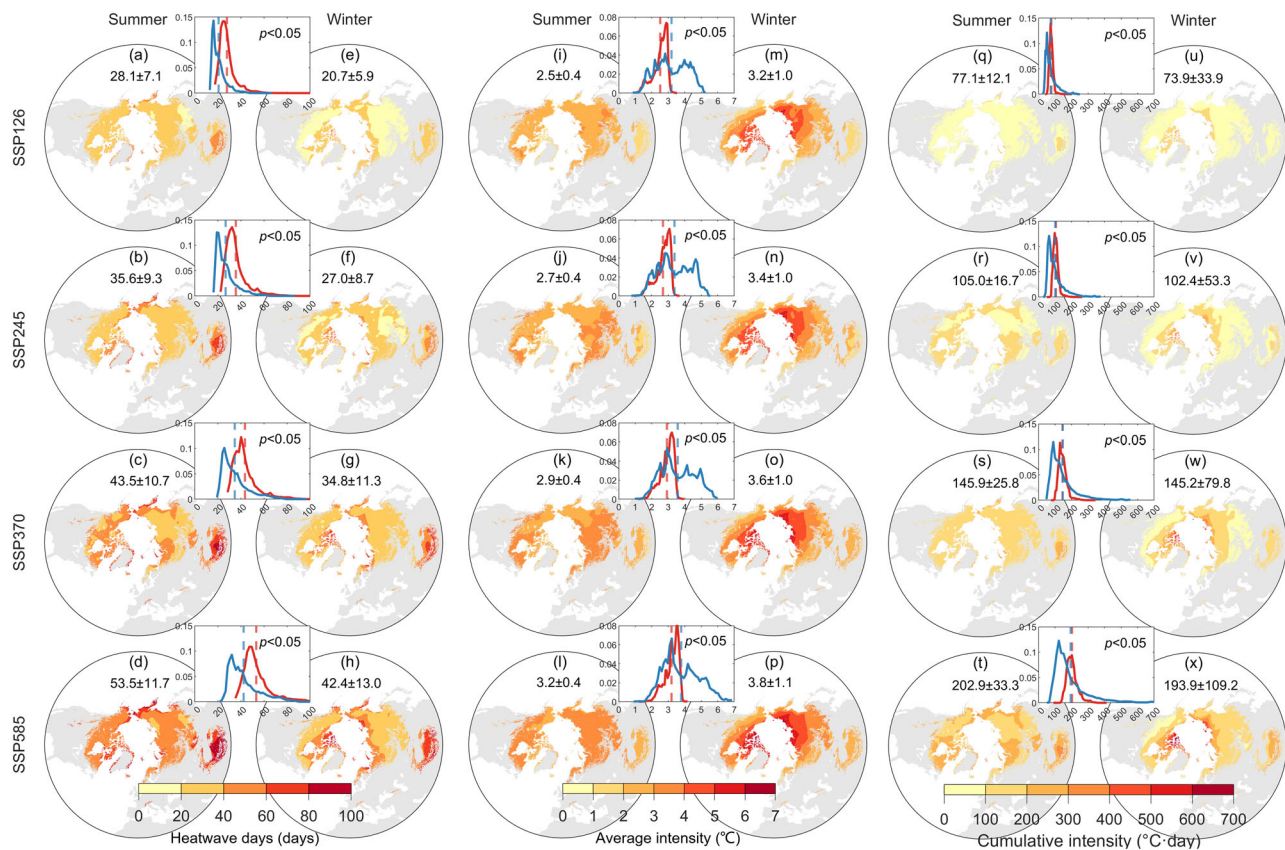


**Fig. 4 | Spatial distributions of multi-year mean heatwave metrics from 2020 to 2100.** The spatial distributions of **a–h** heatwave days (days), **i–p** average intensity ( $^{\circ}\text{C}$ ), and **q–x** cumulative intensity ( $^{\circ}\text{C day}$ ) during summer and winter season under SSP126, SSP245, SSP370, and SSP585 scenarios. Inset boxes represent the

probability distributions of heatwave metrics during the summer (red) and winter (blue) seasons, the significance of the difference between them are indicated by the  $p$ -value. The dash lines represent the mean values of heatwave metrics which are shown on the spatial distribution maps (Mean  $\pm$  SD).

contrasts with the larger heatwave days in the QTP compared to Arctic (Fig. 5a–d).

**Changes in future heatwave metrics.** Figures 6 and 7 represent the spatial and latitudinal patterns of decadal trends in heatwave metrics from 2020 to 2100, respectively. Almost all the permafrost regions show a significantly increasing trends during both summer and winter seasons, particularly under high emission scenarios (Fig. 6a–p). The exception is the average intensity under the SSP126 scenario, where abundant areas show a non-significant trend during summer (9.6%) and winter (47.3%) seasons (Fig. 6i, m). Despite this, the cumulative intensities of summer (winter) heatwaves significantly increase across the PRNH with an average rate of 6.0 (4.5)  $^{\circ}\text{C day}$  per decade under SSP126 scenario, and is expected to rise by a factor of  $\sim 9.3$  ( $\sim 11.6$ ) times under the SSP585 scenario. Overall, the decadal trends in heatwave metrics for the summer season are significantly faster than those for the winter season, as illustrated in the inset boxes in Fig. 6. For example, the heatwave days in the summer season grow 0.8, 1.3, 1.7, and 3.6 day per decade faster than that during the winter season under the SSP126, SSP245, SSP370, and SSP585 scenarios, respectively.

The decadal trends in heatwave metrics vary asymmetrically along latitude, with a lower rate in mid-latitudes and a higher rate in the Arctic and QTP (Fig. 7). Additionally, the trends in summer heatwave days on the QTP are larger than those in the Arctic, whereas the winter heatwave days rise in a comparable rate between the two regions (Fig. 7a–d). The trends in average intensity and cumulative intensity during the winter season in the Arctic are much faster than in other regions. In the mid-latitudes and the QTP, winter heatwave metrics increase more slowly than summer heatwave metrics. Conversely, winter heatwave metrics grow much faster than summer

heatwave metrics in the Arctic, particularly under the SSP370 and SSP585 scenarios (Fig. 7).

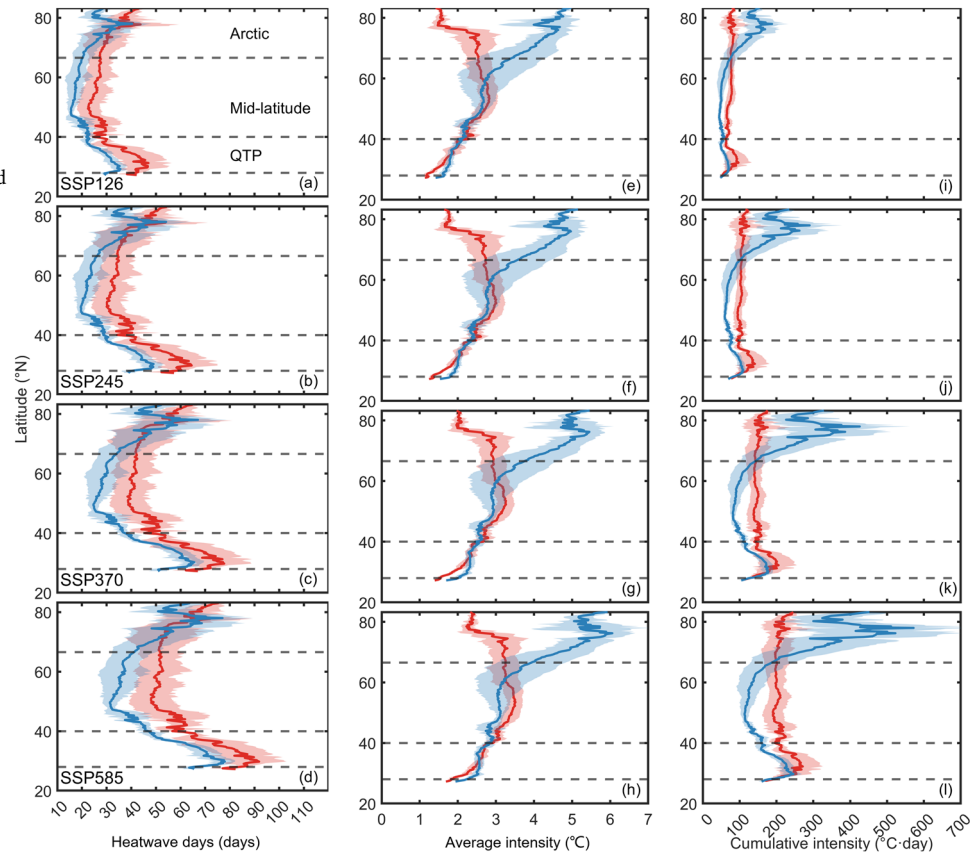
The decadal trends in longest duration and peak intensity have broadly similar spatial and latitudinal distributions with that of heatwave days and average intensity, respectively (Supplementary Figs. 5, 6). The longest duration rises slower than heatwave days (Fig. 6a–h, Supplementary Fig. 5a–h), indicating more frequent and short-lived heatwaves in the future. The peak intensity is expected to increase faster than the average intensity (Fig. 6i–p, Supplementary Fig. 5i–p), which implies us to pay close attention to those high-intensity heatwaves. The trend in longest duration also shows a ‘C-shaped’ curve along latitude as the trend in duration does (Fig. 7a–d), with a comparable rate in the Arctic and QTP (Supplementary Fig. 6a–d). The peak intensity of summer heatwave, however, generally declines with latitude (Supplementary Fig. 6e–h), which is different from the ‘C-shaped’ curve of summer average intensity (Fig. 7e–h).

The rate of increase in heatwave metrics varies with time. Heatwave metrics generally increase at a relatively stable rate from 2020 to 2050. After mid-century, heatwave metrics experience distinct accelerations under the SSP370 and SSP585 scenarios, while relatively stable growth or even downturns are observed under the SSP126 and SSP245 scenarios (Supplementary Fig. 7). This indicates the potential to mitigate and adapt heatwaves and their impacts if immediate actions are taken.

### Heatwaves across different levels of GPs

To investigate the possible impacts of heatwave on infrastructure in permafrost regions, we further examine the behaviors of summer and winter heatwaves over regions with different risk levels of GP for infrastructure damage by the middle of the century (2041–2060). The analysis is conducted

**Fig. 5 | Latitudinal distribution of multi-year mean heatwave metrics from 2020–2100.** The latitudinal distributions of **a–d** heatwave days (days), **e–h** average intensity ( $^{\circ}\text{C}$ ), and **i–l** cumulative intensity ( $^{\circ}\text{C}$  day) during summer (red) and winter (blue) seasons under SSP126, SSP245, SSP370, and SSP585 scenarios. The shaded areas represent the standard deviations across different grids on the same latitude.



over the Northern Hemisphere (NH), the Arctic, the North America (NAM) and the Eurasia (EUA) in the mid-latitude, and the QTP.

Figure 8 shows the statistics of cumulative heatwave intensities across the low, moderate, and high GP levels under the SSP126, SSP245, and SSP585 scenarios. On the whole, the cumulative intensities of summer heatwave in regions with moderate and high GPs are generally higher than those in regions with low GPs, particularly in the Arctic and QTP as well as under the SSP585 scenario. This is consistent with the behaviors of summer heatwave days under different GPs (Supplementary Fig. 8). However, due to the similar heatwave days among GP levels and lower average intensity in high GP level (Supplementary Figs. 8, 9), the winter season generally experience a lower cumulative intensity under the high GP conditions compared with the other two conditions (Fig. 8a–i), except in the EUA and QTP (Fig. 8j–o). Although both summer and winter cumulative intensities on NAM decrease with GPs (Fig. 8g–i), the heatwave days of summer heatwaves and the longest duration of the two seasons increase with GPs (Fig. 9g–i, Supplementary Fig. 8g–i). The winter cumulative intensity between the low and moderate GPs in NAM, as well as among the three GPs in the QTP, shows no significant difference (Fig. 8g–i, m–o). This is because the longer heatwave days in high GPs are offset by the weaker intensity (Supplementary Figs. 8g–i, m–o, 9g–i, m–o). It should be noted that such significance test failures of winter cumulative intensity do not mean little impacts of heatwave on permafrost, since the heatwave days (longest duration) in QTP (NAM) are significantly longer in high GPs than low GPs (Supplementary Fig. 8m–o, Fig. 9i, j).

The summer longest durations generally last distinctly longer in high-GP regions than low- and moderate-GP regions, particularly in the QTP. In contrast, the winter suffers roughly equal longest durations across all three GP levels (Fig. 9). Moreover, the summer is projected to experience similar peak intensities across different GP regions. However, the winter peak intensity is expected to decline with GP levels, except in the EUA and QTP (Supplementary Fig. 10j–o).

These results raise the alarm bells about the impacts of summer heatwaves on the stability of infrastructure across the Northern Hemisphere permafrost areas in the future. Additionally, the role of winter heatwaves should not be neglected, especially in the Eurasia, where the highly unstable permafrost regions are projected to suffer higher winter cumulative intensity and peak intensity.

## Discussion

This study characterizes and compares recent and future summer and winter heatwaves under four SSP scenarios simulated by 18 CMIP6 GCMs across the PRNH. The PRNH has been suffering and is anticipated to experience exacerbated summer and winter heatwaves in the future, and summer heatwave generally occurs more often but with less intensity than winter heatwave (Figs. 2k, l, 4a–p). Heatwaves in the Arctic and the QTP occur more frequently than those in the mid-latitudes (Figs. 2k, 5a–d). The strongest summer heatwaves are found in the mid-latitudes, while the most severe winter heatwaves occur in the Arctic (Figs. 2l, 5e–h). The Arctic has been and will continue to be more affected by winter heatwaves on account of their larger and rapidly increasing intensity (Figs. 2k, l, 5e–l, 6e–h). In contrast to experiencing more winter heatwaves in the past decades (Fig. 2m), the QTP in the future is expected to face greater summer heatwaves in the future due to their longer and fast-growing heatwave days (Figs. 5a–d, i–l, 6a–d). Investigations on heatwaves across different GP levels demonstrate that the PRNH with high GPs tend to face more pressure from summer heatwaves, and the high-GP areas in Eurasia will bear more severe winter heatwaves (Figs. 8, 9).

This study used the NEX-GDDP-CMIP6 data to characterize the future heatwaves. The dataset is bias-corrected and downscaled from GCM outputs of CMIP6<sup>44,45</sup>, making it more realistic for reproducing heatwave properties than its predecessor CMIP5 dataset, especially in the high northern latitudes<sup>46,47</sup>. This makes it widely used in studies of climate change<sup>48–50</sup>. In this study, we use the ensemble mean of heatwave properties



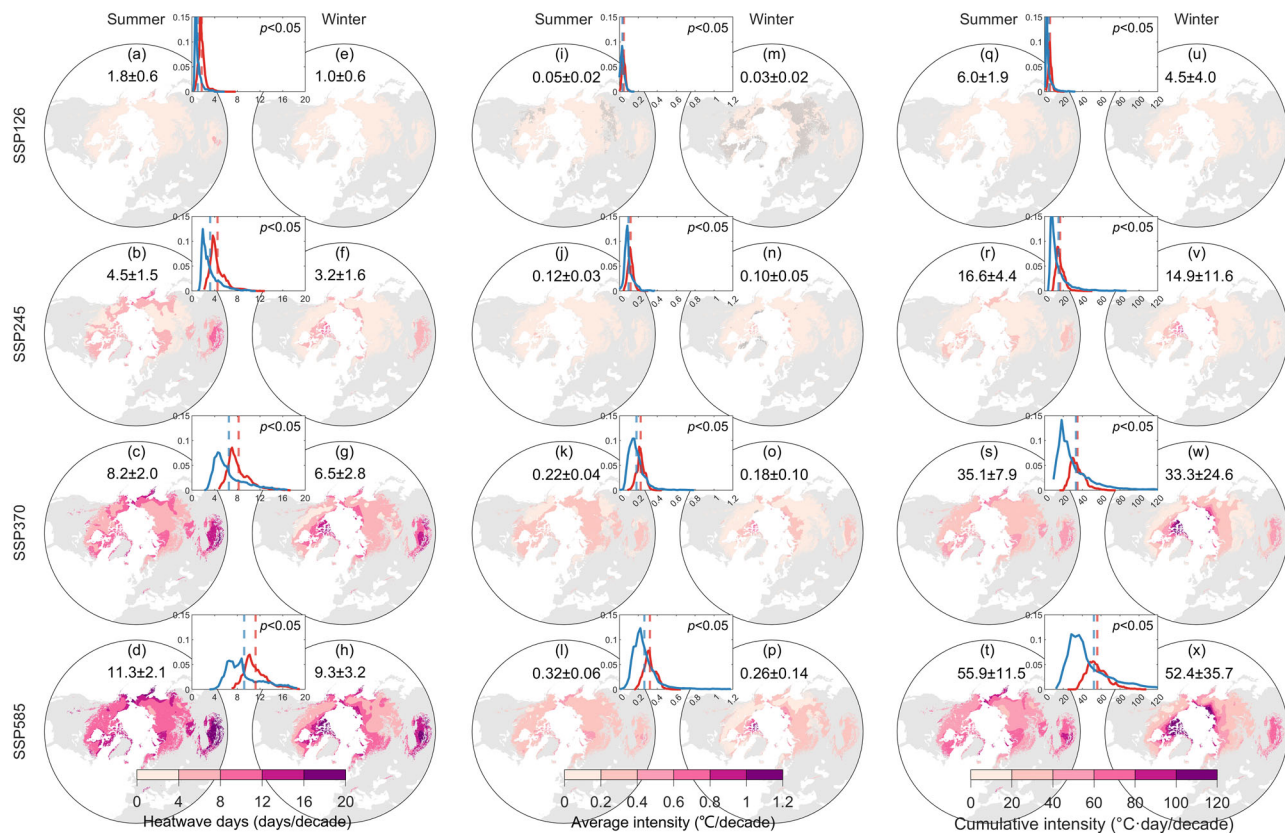


**Fig. 6 | Spatial distributions of decadal trends multi-year mean heatwave metrics from 2020 to 2100.** Spatial distributions of decadal trends in a–h heatwave days (days/decade), i–p average intensity (°C/decade), and q–x cumulative intensity (°C day/decade) during summer and winter seasons under the SSP126, SSP245, SSP370, and SSP585 scenarios. All grid cells are significantly increasing with  $p < 0.05$

except those dotted with gray dots. Inset boxes represent the probability distributions of trends in heatwave metrics during the summer (red) and winter (blue) seasons, the significance of the difference between them are indicated by the  $p$ -value. The dashed lines represent the mean values of heatwave metrics which are shown spatial distribution maps (Mean ± SD).

across 18 GCMs to further minimize uncertainties<sup>51</sup>. The exacerbated heatwaves detected in the past decades in this study are in accord with the rapid development of heatwaves in the NH since the 1950s<sup>14,24,43,52,53</sup>. Given the continued warming of air temperature over the PRNH under future climate change<sup>54</sup>, heatwaves are virtually certain to become more frequent and intense, as demonstrated in this study and others<sup>55–59</sup>. Moreover, the warming trend of temperature is suggested to slow down under the SSP126 and SSP245 scenarios as climate forcing stabilizes from 2050 to 2074<sup>60</sup>, while exhibiting a faster positive trend under the SSP585 scenario compared to low-emission scenarios<sup>54,61</sup>. This aligns with the relatively stable growth of heatwave metrics after the 2050 s under the SSP126 and SSP245 scenarios, and an accelerating increase under the SSP370 and SSP585 scenarios (Supplementary Fig. 7).

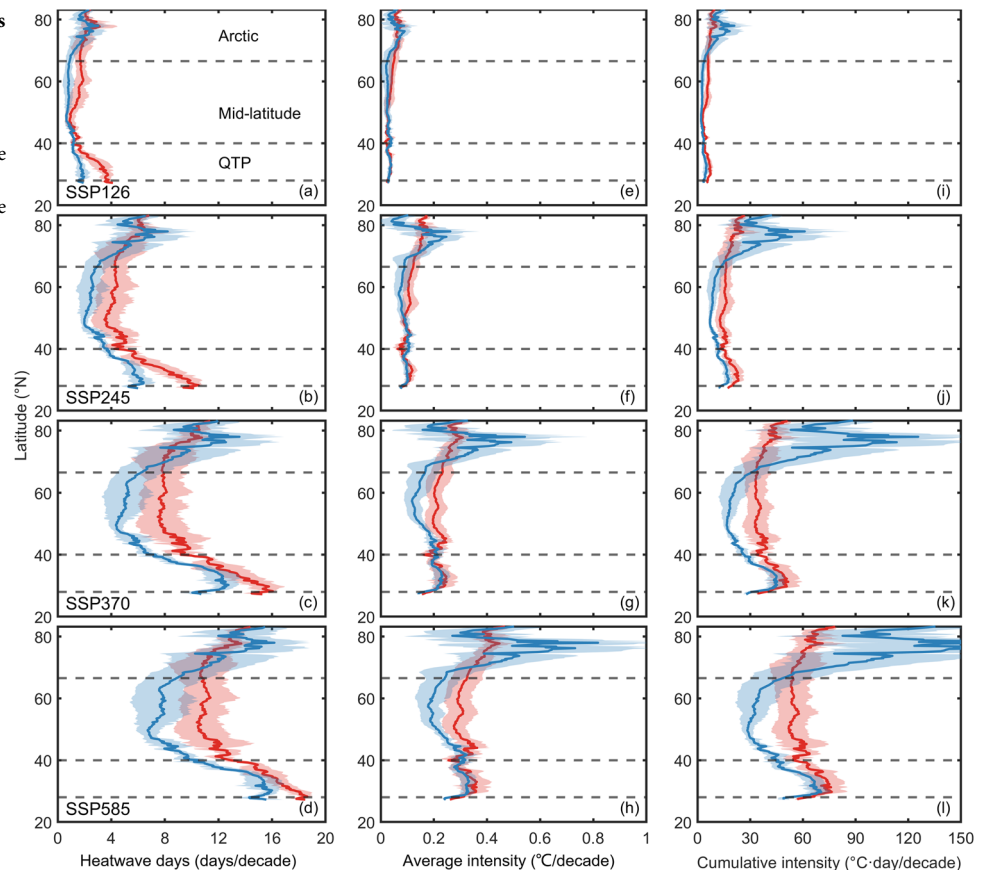
We demonstrate a latitudinal difference of heatwave behaviors (Figs. 2, 5, 6). The ‘C-shaped’ latitudinal distributions of heatwave days are in agreement with the distribution of warm spell duration<sup>56</sup>, which is partly related to the fact that QTP and the Arctic have warmed approximately 2 and 4 times as fast as the global average, respectively<sup>36,37,62,63</sup>. In the mid-latitudes, heatwaves are closely associated with the disproportional enhancement of air temperature in the Arctic—a phenomenon known as Arctic amplification<sup>64</sup>. Arctic amplification is favorable to more occurrence of summer heatwaves in mid-latitudes by driving atmospheric circulations over surrounding continents<sup>65,66</sup>. In winter, there is a contrast between Arctic warming and Eurasia cooling, which has been widely identified by observations and model simulations<sup>67,68</sup>. This may partly explain the less occurrence of winter heatwave in mid-latitudes compared with other permafrost regions (Fig. 5a–d). In addition, heatwaves in mid-latitudes are also closely linked to local land surface conditions (e.g., soil moisture, snow cover, and deforestation), which has been shown to promote and prolong

heatwaves by disturbing the surface energy partition process and elevating air temperatures<sup>69–72</sup>. Permafrost regions are featured with cold climate and are home to the Earth’s cryosphere system. This region is suffering degradation of permafrost and snow cover as well as significant wildfires<sup>73,74</sup>. This may contribute to dry out and dark the surface soil<sup>75,76</sup>, and set stage for heatwave occurrence. Those complex mechanisms suggest a difficulty in attributing and predicting the occurrence of heatwaves over the mid-latitudes<sup>77,78</sup>.

The average intensity of summer heatwaves in the past and future follow the latitudinal distributions of the mean annual air temperature in the PRNH<sup>54</sup>. The latitudinal decline of winter average intensity is consistent with the strength of near-surface air temperature over the Arctic to lower latitudes<sup>54,79,80</sup>, as well as the projected spatial patterns of changes in annual minimum daily minimum temperature (TNn) of the Northern Hemisphere<sup>56,59</sup>. The substantially high winter temperature and increase rate at higher latitudes can be attributed to the dramatic shrinking snow cover and sea ice<sup>64,81,82</sup>.

For the first time, the study underscores the dynamics of winter heatwaves over the PRNH. Similar to summer heatwaves, winter heatwaves in the future are expected to become more frequent and stronger as expected. This matches those observed in previous studies<sup>38,83,84</sup> and the increasingly reported abnormal winter heatwaves in recent years<sup>83,85–88</sup>. Despite winter average temperature in the last decades is detected to warm at a faster rate than summer over cold regions<sup>79</sup>, with general larger growth in minimum than maximum temperatures<sup>89</sup>, winter heatwaves tend to have a shorter heatwave days with a greater intensity than summer heatwaves (Figs. 2, 4). More specifically, the rapid increase in winter temperatures is not expected to induce more frequent and stronger winter heatwaves than summer heatwaves in the mid-latitudes and QTP, but may lead to a

**Fig. 7 | Latitudinal distribution of decadal trends in multi-year mean heatwave metrics from 2020 to 2100.** The latitudinal distributions of decadal trends in **a–d** heatwave days (days/decade), **e–h** average intensity ( $^{\circ}\text{C}/\text{decade}$ ), and **i–l** cumulative intensity ( $^{\circ}\text{C day}/\text{decade}$ ) during the summer (red) and winter (blue) seasons under the SSP126, SSP245, SSP370, and SSP585 scenarios. The shaded areas represent the standard deviations across different grids on the same latitude.



significantly high winter heatwave intensity in the Arctic (Figs. 5, 6). These findings extended our knowledge of winter heatwave's behavior in a warming world. Note that, according to our definition, the temperatures during winter heatwave days can be sub-zero, yet they still significantly impact permafrost. A warmer winter favors higher ground temperatures at the onset of the subsequent thawing season, allowing more energy to contribute directly to soil temperature and active layer development in the following summer. This has been verified by numerous studies in thin-snow covered areas in polar regions such as Alaska, northern Canada, Nordic sites, as well as mountain regions like the QTP<sup>37,90–92</sup>. In addition, abnormally high winter temperature can rapidly melt snow, as snowpack is extremely sensitive to temperatures exceeding  $-8^{\circ}\text{C}$ <sup>93</sup>. The resulting meltwater infiltrates into the surface soil and influences soil thawing in the spring<sup>41</sup>. Moreover, winter heatwaves may contribute to the variations of unfrozen water content of frozen soil (Supplementary Fig. 11), by direct heat transfer and/or changes in snowpacks<sup>94</sup>, which is critical for water redistribution, deformation during freeze-thaw process, and frozen soil strength in cold regions<sup>95,96</sup>. Furthermore, carbon decomposition can occur at temperatures well below freezing in cold soils<sup>97–99</sup>, releasing vast amounts of carbon dioxide that may offset the carbon uptake by plants<sup>98</sup>. Despite the hitherto unknown impacts of winter heatwaves on soil carbon balance, it is plausible that winter heatwaves can be significant contributors to carbon fluxes, given that soil temperature and unfrozen water content are the two main drivers of winter soil carbon flux<sup>98</sup>, both closely related to winter heatwaves.

This study provides new insights into the possible behaviors and impacts of heatwaves across different geohazard risk levels, which can be a reference for stakeholders to identify infrastructure vulnerabilities and implement resilient solutions in a warming world. The high-risk-level area are mainly located in the southern part of permafrost regions (Supplementary Fig. 1), where the permafrost temperature is high and sensitive to climate change, one could expect greater impact of heatwaves on stability for infrastructure in those regions<sup>100</sup>. Despite less severe heatwaves can be offset

by the land surface layers, extreme heatwaves like the 2003 European heatwave and 2020 Siberia heatwave could enhance the inter-annual variations of soil temperature and seasonal thaw depth<sup>20–23</sup>, which may cause uneven ground settlement and thus instability for infrastructure<sup>101</sup>. Heatwaves are expected to be more extreme and uncertain in the future, which will put infrastructure at higher risk of failure and increase the maintenance costs. Moreover, the nonlinear heatwaves superimposed on a gradual warming are likely to threaten the infrastructures already in place by triggering abrupt thaw events<sup>102,103</sup>. It is noteworthy that heatwaves could also influence infrastructure indirectly by triggering catastrophic snowmelt floods and wildfires. They may not only cause permafrost thaw, thermokarst development (e.g., water impoundment, talik initiation), and thus threaten the safety of infrastructure, but also destroy roads, bridges, buildings in a short period of time, causing massive losses<sup>104,105</sup>. More efforts should be paid in the future on quantifying the implications of heatwaves on the hydrothermal processes of permafrost. Although several studies have extended our knowledge of the response of permafrost to heatwaves, most of them were conducted at a site scale and/or mainly focused on the detection of co-relationship<sup>19,20,23,24,27,42,106,107</sup>. Significant knowledge gaps remain regarding the processes and mechanisms of the influence of heatwave metrics (e.g., timing, duration, intensity) on the hydrothermal conditions of permafrost soils. Continued investigation with a broad spectrum of climate and environmental conditions using physical numeric models is required to make an objective, overall and rational conclusion.

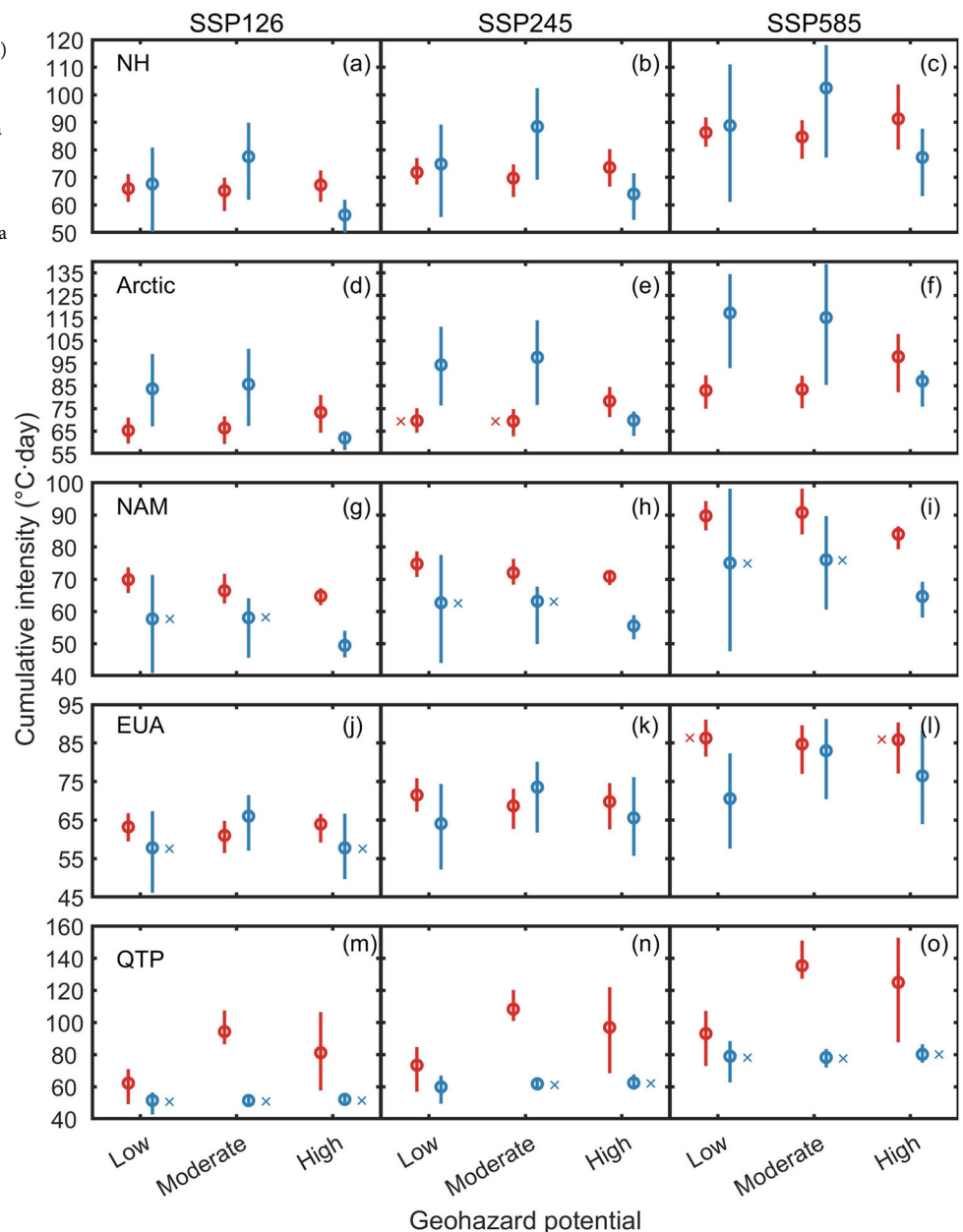
## Methods

### Data

Daily maximum near-surface air temperature ( $T_{\text{max}}$ ) is employed to identify heatwaves.  $T_{\text{max}}$  was obtained from the NASA Earth Exchange (NEX) Global Daily Downscaled Projections (GDDP) dataset (NEX-GDDP-CMIP6), which compiles global climate variables derived from the General Circulation Model (GCM) runs conducted under the Coupled Model



**Fig. 8 | Heatwave cumulative intensities across different geohazard potential levels.** Summer (red) and winter (blue) heatwave cumulative intensities over the **a–c** Northern Hemisphere (NH), **d–f** Arctic, **g–i** North America (NAM), **j–l** Eurasia (EUA), and **m–o** Qinghai-Tibetan Plateau (QTP) under the SSP126, SSP245, and SSP585 scenarios. The limits of statistics indicate the 75% and 25% percentiles, and the circles are the mean values. For a given season, all the statistics are significantly different from each other, except those labeled with cross marks.



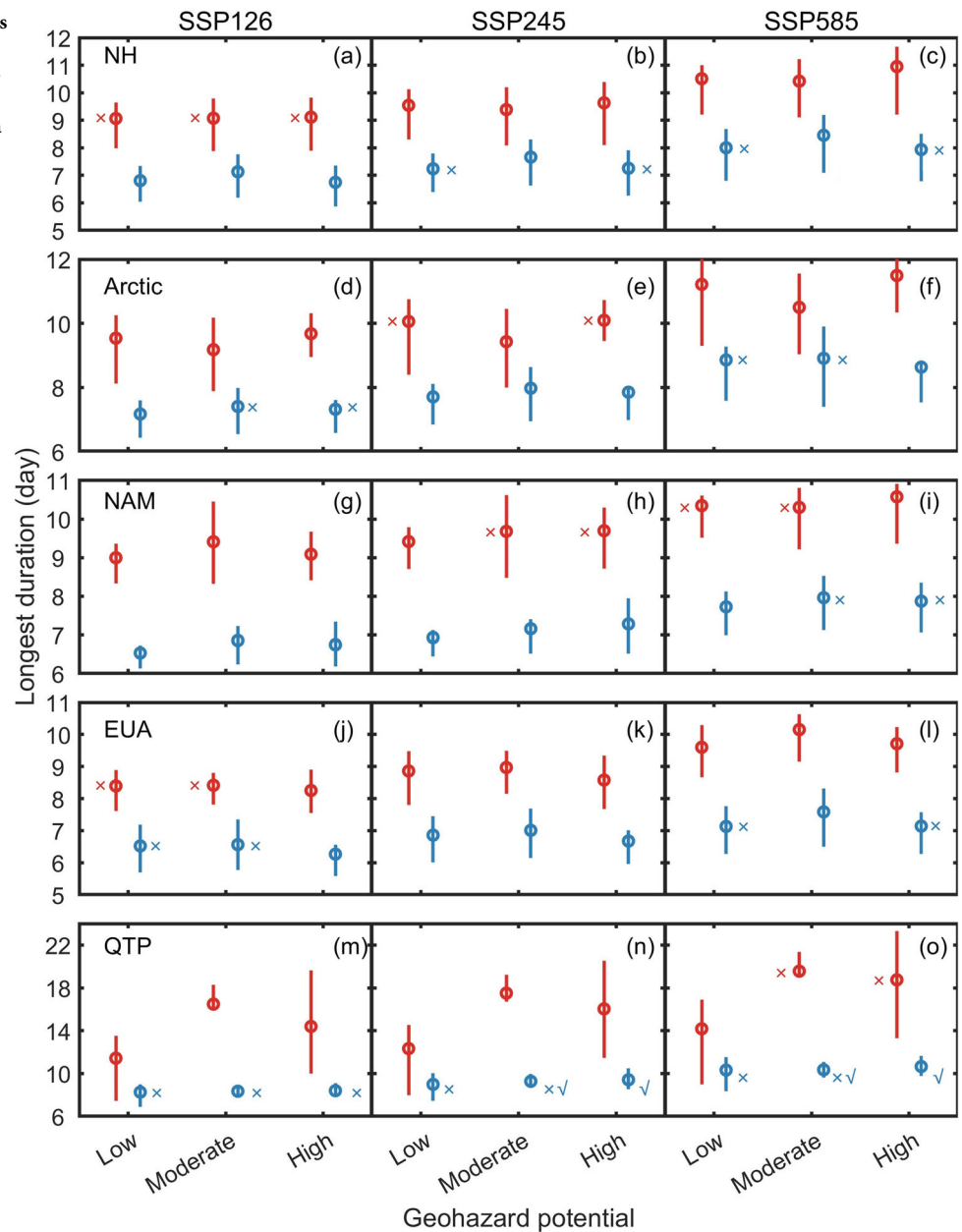
Intercomparison Project Phase 6 (CMIP6). The NEX-GDDP-CMIP6 dataset includes climate projections (2015–2100) from 35 CMIP6 GCMs and 4 greenhouse gas emissions scenarios known as Shared Socioeconomic Pathways (SSPs), as well as the historical experiment for each model (1950–2014). Each of the historical and projected time series was bias-corrected using an observational climate data from the Global Meteorological Forcing Dataset (GMFD) for Land Surface Modeling<sup>108</sup>, and downscaled to a spatial resolution of 0.25-degree<sup>109</sup>.

Using the NEX-GDDP-CMIP6 data, we assessed heatwaves during two seasons: the summer (May to September) and winter (November to next March), across the PRNH for the recent decades (1980–2014) and future period (2021–2100) under four combined scenarios (SSP1-2.6, SSP2-4.5, SSP3-7.0, and SSP5-8.5). The first realization (i.e., ‘r1i1p1f1’) of 18 CMIP6 GCMs were adopted as listed in Table 1.

The Northern Hemisphere permafrost region was resampled from the permafrost probability map of Obu et al.<sup>1</sup>. The study area was classified as the Arctic (66°34'N ~ 90°N), the mid-latitude (40°N ~ 66°34'N) and the Qinghai-Tibetan Plateau (QTP, 28°N ~ 40°N) to figure out the regional difference of heatwaves (Fig. 1a).

To investigate the possible effects of heatwaves on infrastructure, a map depicting the geohazard potentials (GPs) for infrastructure damage was adopted to investigate the behaviors of heatwaves in different risk levels<sup>110</sup>. The GPs were projected for the period of 2041–2060 under three climate-forcing scenarios (Representative Concentration Pathways 2.6, 4.5 and 8.5). A pre-classification was conducted separately using three different hazard evaluation models: the settlement index, the risk zonation index, and the analytic hierarchy process-based index. These indices considered factors such as climate warming, permafrost conditions (e.g., soil properties, ground ice content, topography), and expert knowledge. The results from the three indices were then consolidated through a majority-vote approach in a consensus index, which was used in the final classification of GPs (Supplementary Fig. 2). The GP level (low, moderate, and high) of each grid cell was classified based on the following criteria: if two or three of the indices shared a hazard value, that value was recorded to represent consensus. When all three indices had different values, the risk level was manually set as a moderate hazard value. In this study, the datasets were upsampled from 30 arc-second to 0.25-degree by performing a majority vote

**Fig. 9 | The longest durations of heatwaves across different geohazard potential levels.** The longest durations of summer (red) and winter (blue) heatwaves over the a–c Northern Hemisphere (NH), d–f Arctic, g–i North America (NAM), j–l Eurasia (EUA), and m–o Qinghai-Tibetan Plateau (QTP) under SSP126, SSP245, and SSP585 scenarios. The limits of statistics indicate the 75% and 25% percentiles and the circles are the mean values. For a given season, all the statistics are significantly different from each other, except those labeled with cross marks or check marks.



procedure within a 30×30 window using the ArcMap's Block Statistics tool (Supplementary Fig. 1).

### Heatwave identification

In this study, a heatwave is identified for each grid when at least three consecutive days have maximum temperatures ( $T_{\max}$ ) above the threshold temperature. Threshold temperature is localized both spatially and temporally. Specifically, the threshold temperatures for each calendar day are specified as the 90th percentile ( $T_{90}$ ) of  $T_{\max}$  from the baseline period of 1980–2014. To reduce seasonality effects,  $T_{\max}$  records are constructed using a 15-day window centered around the calendar day of interest (Fig. 1b). For example, for August 8 at a given grid, the  $T_{\max}$  values from August 1 to August 15 over all 35 years (1980–2014) are retrieved, resulting in a total of 525 samples (35 years × 15 days). The threshold temperature is then calculated as the 90th percentile ( $T_{90}$ ) of these 525 samples. This method enables the detection of both summer and winter heatwaves<sup>11</sup>.

The conceptual diagram of heatwave metrics is shown as Fig. 1c. A heatwave can be characterized by duration and intensity (sum of  $T_{\max} - T_{90}$ ),

which defines how long and how severe a heatwave event is, respectively (Fig. 1c). For each season, heatwave is characterized by heatwave days, average intensity, and cumulative intensity. Heatwave days are the sum of durations of all heatwaves. Average intensity is the average intensity of heatwaves across the season and is calculated as the sum of  $T_{\max} - T_{90}$  over all heatwave days. Cumulative intensity is the sum of heatwave intensity of all heatwave events, which can serve as the total heatwave stress the season bears. We also identified the extreme heatwaves, i.e., the longest and hottest heatwaves, which are characterized using the longest duration and peak intensity, respectively. The longest duration is the total heatwave days of the longest heatwave event, and the peak density is the maximum  $T_{\max} - T_{90}$  of the heatwave event with max intensity. Each metric is calculated for the summer (May–September) and winter season (November to next March) at each grid cell. For regional analysis, seasonal metrics are spatially averaged accordingly.

All the trends are calculated at the 5% level based on the Mann-Kendall non-parametric test and Sen's slope estimator, which is nonparametric and robust against outliers. A Tukey-test is used to examine the whether the difference is significant between data series.

**Table 1 | Information of the NEX-GDDP-CMIP6 dataset from 18 GCMs**

No.	Model	Institution
1	ACCESS-CM2	CSIRO, Australia
2	ACCESS-ESM1-5	CSIRO, Australia
3	BCC-CSM2-MR	Beijing Climate Center, China
4	CanESM5	CCCma, Canada
5	CMCC-ESM2	Fondazione Centro Euro-Mediterraneo sui Cambiamenti Climatici, Italy
6	EC-Earth3	EC-Earth-Consortium, Europe
7	EC-Earth3-Veg-LR	EC-Earth-Consortium, Europe
8	GFDL-ESM4	NOAA-GFDL, the US
9	INM-CM4-8	INM, Russia
10	INM-CM5-0	INM, Russia
11	IPSL-CM6A-LR	IPSL, France
12	KACE-1-0-G	NIMS-KMA, South Korea
13	MIROC6	MIROC, Japan
14	MPI-ESM1-2-HR	DKRZ, Germany
15	MPI-ESM1-2-LR	DKRZ, Germany
16	MRI-ESM2-0	MRI, Japan
17	NorESM2-LM	NCC, Norway
18	NorESM2-MM	NCC, Norway

### Data availability

Data in this study can be reached at: (a) NEX-GDDP-CMIP6: <https://www.nccs.nasa.gov/services/data-collections/land-based-products/nex-gddp-cmip6>; (b) Permafrost probability map: <https://pangaea.de/10.1594/PANGAEA.888600>; (c) Geohazard potential maps: <https://pangaea.de/10.1594/PANGAEA.893881>.

### Code availability

The source codes of this study are available from the corresponding author upon reasonable request.

Received: 4 September 2024; Accepted: 6 April 2025;

Published online: 17 April 2025

### References

- Obu, J. et al. Northern Hemisphere permafrost map based on TTOP modelling for 2000–2016 at 1 km<sup>2</sup> scale. *Earth Sci. Rev.* **193**, 299–316 (2019).
- Biskaborn, B. K. et al. Permafrost is warming at a global scale. *Nat. Commun.* **10**, 264 (2019).
- Peng, X. et al. Active layer thickness and permafrost area projections for the 21st century. *Earths Future* **11**, e2023EF003573 (2023).
- Zhao, L. et al. Changing climate and the permafrost environment on the Qinghai–Tibet (Xizang) plateau. *Permafr. Periglac. Process.* **31**, 396–405 (2020).
- Olefeldt, D. et al. Circumpolar distribution and carbon storage of thermokarst landscapes. *Nat. Commun.* **7**, 13043 (2016).
- Jorgenson, M. T. in *Treatise on Geomorphology (Second Edition)* (ed. Shroder, J. F.) 392–414 (Academic Press, 2022).
- Chen, X. et al. Different responses of surface freeze and thaw phenology changes to warming among Arctic permafrost types. *Remote Sens. Environ.* **272**, 112956 (2022).
- Zhang, T., Barry, R. G., Knowles, K., Heginbottom, J. A. & Brown, J. Statistics and characteristics of permafrost and ground-ice distribution in the Northern Hemisphere. *Polar Geogr.* **31**, 47–68 (2008).
- Ping, C. L., Jastrow, J. D., Jorgenson, M. T., Michaelson, G. J. & Shur, Y. L. Permafrost soils and carbon cycling. *SOIL* **1**, 147–171 (2015).
- Vonk, J. E. et al. Reviews and syntheses: effects of permafrost thaw on Arctic aquatic ecosystems. *Biogeosciences* **12**, 7129–7167 (2015).
- Gao, H. et al. Permafrost hydrology of the Qinghai-Tibet Plateau: a review of processes and modeling. *Front. Earth Sci.* **8**, <https://doi.org/10.3389/feart.2020.576838> (2021).
- Hjort, J. et al. Impacts of permafrost degradation on infrastructure. *Nat. Rev. Earth Environ.* **3**, 24–38 (2022).
- Schuur, E. A. G. et al. Permafrost and climate change: carbon cycle feedbacks from the warming Arctic. *Annu. Rev. Environ. Resour.* **47**, 343–371 (2022).
- Perkins-Kirkpatrick, S. E. & Lewis, S. C. Increasing trends in regional heatwaves. *Nat. Commun.* **11**, 3357 (2020).
- Matters, P. P. Is Alaska Prepared For Extreme Wildfires? <https://blogs.helmholtz.de/polarpredictionmatters/2020/11/is-alaska-prepared-for-extreme-wildfires/> (2020).
- Schreiber, M. The Massive Norilsk Fuel Spill Could be Linked to Permafrost Thaw, A Growing Threat to Arctic Infrastructure. <https://www.arctictoday.com/the-massive-norilsk-fuel-spill-could-be-linked-to-permafrost-thaw-a-growing-threat-to-arctic-infrastructure/> (2020).
- Irfan, U. The North Pole just had an extreme heat wave for the 3rd winter in a row. <https://www.vox.com/energy-and-environment/2018/2/27/17053284/arctic-heat-wave-north-pole-climate> (2018).
- WMO. WMO recognizes new Arctic temperature record of 38°C. <https://wmo.int/media/news/wmo-recognizes-new-arctic-temperature-record-of-380c> (2021).
- Atkinson, D. E. et al. Canadian cryospheric response to an anomalous warm summer: a synthesis of the climate change action fund project “the state of the arctic cryosphere during the extreme warm summer of 1998. *Atmos. Ocean* **44**, 347–375 (2006).
- Isaksen, K., Benestad, R. E., Harris, C. & Solli, J. L. Recent extreme near-surface permafrost temperatures on Svalbard in relation to future climate scenarios. *Geophys. Res. Lett.* **34**, <https://doi.org/10.1029/2007GL031002> (2007).
- Hilbich, C. et al. Monitoring mountain permafrost evolution using electrical resistivity tomography: a 7-year study of seasonal, annual, and long-term variations at Schilthorn, Swiss Alps. *J. Geophys. Res. Earth Surf.* **113**, <https://doi.org/10.1029/2007JF000799> (2008).
- Blanchet, J. & Davison, A. C. Statistical modelling of ground temperature in mountain permafrost. *Proc. R. Soc. A Math. Phys. Eng. Sci.* **468**, 1472–1495 (2012).
- Zhu, X. et al. Non-negligible contribution to seasonally thawing depth of active layer from extreme Warming events in the Tanggula permafrost region of Qinghai-Tibet Plateau. *J. Geophys. Res. Atmos.* **126**, e2021JD035088 (2021).
- Zhu, X. et al. Increased extreme warming events and the differences in the observed hydrothermal responses of the active layer to these events in China’s permafrost regions. *Clim. Dyn.* **59**, 785–804 (2022).
- Balser, A. W., Jones, J. B. & Gens, R. Timing of retrogressive thaw slump initiation in the Noatak Basin, northwest Alaska, USA. *J. Geophys. Res. Earth Surf.* **119**, 1106–1120 (2014).
- Gruber, S. & Haeberli, W. Permafrost in steep bedrock slopes and its temperature-related destabilization following climate change. *J. Geophys. Res. Earth Surf.* **112**, <https://doi.org/10.1029/2006JF000547> (2007).
- Luo, J. et al. Inventory and frequency of retrogressive thaw slumps in permafrost region of the Qinghai–Tibet Plateau. *Geophys. Res. Lett.* **49**, e2022GL099829 (2022).
- Qin, Y., Lu, P. & Wu, J. Mapping thermokarst lakes in different physical states on the central Tibetan plateau. *Int. J. Digital Earth* **16**, 4296–4316 (2023).



29. Huggel, C. et al. Recent and future warm extreme events and high-mountain slope stability. *Philos. Trans. R. Soc. A Math. Phys. Eng. Sci.* **368**, 2435–2459 (2010).
30. Schuur, E. A. G. & Mack, M. C. Ecological response to permafrost thaw and consequences for local and global ecosystem services. *Annu. Rev. Ecol. Syst.* **49**, 279–301 (2018).
31. Turetsky, M. R. et al. Carbon release through abrupt permafrost thaw. *Nat. Geosci.* **13**, 138–143 (2020).
32. Froitzheim, N., Majka, J. & Zastrow, D. Methane release from carbonate rock formations in the Siberian permafrost area during and after the 2020 heat wave. *Proc. Natl Acad. Sci. USA* **118**, e2107632118 (2021).
33. Schuur, E. A. G. et al. Climate change and the permafrost carbon feedback. *Nature* **520**, 171–179 (2015).
34. Luo, D. et al. Thermal regime of warm-dry permafrost in relation to ground surface temperature in the Source Areas of the Yangtze and Yellow rivers on the Qinghai-Tibet Plateau, SW China. *Sci. Total Environ.* **618**, 1033–1045 (2018).
35. Jacques-Dumas, V., Ragone, F., Borgnat, P., Abry, P. & Bouchet, F. Deep learning-based extreme heatwave forecast. *Front. Clim.* **4**, <https://doi.org/10.3389/fclim.2022.789641> (2022).
36. Rantanen, M. et al. The Arctic has warmed nearly four times faster than the globe since 1979. *Commun. Earth Environ.* **3**, 168 (2022).
37. Zhang, G., Nan, Z., Yin, Z. & Zhao, L. Isolating the contributions of seasonal climate warming to permafrost thermal responses over the Qinghai-Tibet Plateau. *J. Geophys. Res. Atmos.* **126**, e2021JD035218 (2021).
38. Graham, R. M. et al. Increasing frequency and duration of Arctic winter warming events. *Geophys. Res. Lett.* **44**, 6974–6983 (2017).
39. Leach, N. J., Weisheimer, A., Allen, M. R. & Palmer, T. Forecast-based attribution of a winter heatwave within the limit of predictability. *Proc. Natl Acad. Sci. USA* **118**, e2112087118 (2021).
40. Collow, A. B. M. et al. Seasonal variability in the mechanisms behind the 2020 Siberian heatwaves. *J. Clim.* **35**, 3075–3090 (2022).
41. Pavlovskii, I., Hayashi, M. & Itenfisu, D. Midwinter melts in the Canadian prairies: energy balance and hydrological effects. *Hydrol. Earth Syst. Sci.* **23**, 1867–1883 (2019).
42. Hansen, B. B. et al. Warmer and wetter winters: characteristics and implications of an extreme weather event in the High Arctic. *Environ. Res. Lett.* **9**, 114021 (2014).
43. Walsh, J. E. et al. Extreme weather and climate events in northern areas: a review. *Earth Sci. Rev.* **209**, 103324 (2020).
44. Teufel, B. & Sushama, L. Abrupt changes across the Arctic permafrost region endanger northern development. *Nat. Clim. Change* **9**, 858–862 (2019).
45. Thrasher, B., Maurer, E. P., McKellar, C. & Duffy, P. B. Technical note: Bias correcting climate model simulated daily temperature extremes with quantile mapping. *Hydrol. Earth Syst. Sci.* **16**, 3309–3314 (2012).
46. Chen, H., Sun, J., Lin, W. & Xu, H. Comparison of CMIP6 and CMIP5 models in simulating climate extremes. *Sci. Bull.* **65**, 1415–1418 (2020).
47. Al-Yaari, A., Zhao, Y., Cheruy, F. & Thiery, W. Heatwave characteristics in the recent climate and at different global warming levels: a multimodel analysis at the global scale. *Earths Future* **11**, e2022EF003301 (2023).
48. Park, T. et al. What does global land climate look like at 2°C warming? *Earth's Future* **11**, e2022EF003330 (2023).
49. Murali, G., Iwamura, T., Meiri, S. & Roll, U. Future temperature extremes threaten land vertebrates. *Nature* **615**, 461–467 (2023).
50. Li, H., Pan, X., Washakh, R. M. A. & Nie, X. A new method of diagnosing the historical and projected changes in permafrost on the Tibetan Plateau. *Earths Future* **12**, e2023EF003897 (2024).
51. Sillmann, J., Kharin, V. V., Zhang, X., Zwiers, F. W. & Bronaugh, D. Climate extremes indices in the CMIP5 multimodel ensemble: part 1. Model evaluation in the present climate. *J. Geophys. Res. Atmos.* **118**, 1716–1733 (2013).
52. Barriopedro, D., García-Herrera, R., Ordóñez, C., Miralles, D. G. & Salcedo-Sanz, S. Heat waves: physical understanding and scientific challenges. *Rev. Geophys.* **61**, e2022RG000780 (2023).
53. Dobricic, S., Russo, S., Pozzoli, L., Wilson, J. & Vignati, E. Increasing occurrence of heat waves in the terrestrial Arctic. *Environ. Res. Lett.* **15**, 024022 (2020).
54. Hu, G. et al. Continued warming of the permafrost regions over the Northern Hemisphere under future climate change. *Earths Future* **10**, e2022EF002835 (2022).
55. Landrum, L. & Holland, M. M. Extremes become routine in an emerging new Arctic. *Nat. Clim. Change* **10**, 1108–1115 (2020).
56. Sillmann, J., Kharin, V. V., Zwiers, F. W., Zhang, X. & Bronaugh, D. Climate extremes indices in the CMIP5 multimodel ensemble: part 2. Future climate projections. *J. Geophys. Res. Atmos.* **118**, 2473–2493 (2013).
57. Zhang, G., Zeng, G., Yang, X. & Jiang, Z. Future changes in extreme high temperature over China at 1.5 °C–5 °C global warming based on CMIP6 simulations. *Adv. Atmos. Sci.* **38**, 253–267 (2021).
58. Almazroui, M. et al. Projected changes in climate extremes using CMIP6 simulations over SREX regions. *Earth Syst. Environ.* **5**, 481–497 (2021).
59. Li, C. et al. Changes in annual extremes of daily temperature and precipitation in CMIP6 models. *J. Clim.* **34**, 3441–3460 (2021).
60. Fan, X., Duan, Q., Shen, C., Wu, Y. & Xing, C. Global surface air temperatures in CMIP6: historical performance and future changes. *Environ. Res. Lett.* **15**, 104056 (2020).
61. Yang, X., Zhou, B., Xu, Y. & Han, Z. CMIP6 evaluation and projection of temperature and precipitation over China. *Adv. Atmos. Sci.* **38**, 817–830 (2021).
62. Wang, Q., Fan, X. & Wang, M. Evidence of high-elevation amplification versus Arctic amplification. *Sci. Rep.* **6**, 19219 (2016).
63. Francis, J. & Skific, N. Evidence linking rapid Arctic warming to mid-latitude weather patterns. *Philos. Trans. R. Soc. A Math. Phys. Eng. Sci.* **373**, 20140170 (2015).
64. Previdi, M., Smith, K. L. & Polvani, L. M. Arctic amplification of climate change: a review of underlying mechanisms. *Environ. Res. Lett.* **16**, 093003 (2021).
65. Vavrus, S. J. The influence of Arctic amplification on mid-latitude weather and climate. *Curr. Clim. Change Rep.* **4**, 238–249 (2018).
66. Cohen, J. et al. Recent Arctic amplification and extreme mid-latitude weather. *Nat. Geosci.* **7**, 627–637 (2014).
67. Xie, Y., Wu, G., Liu, Y., Huang, J. & Nie, H. A dynamic and thermodynamic coupling view of the linkages between Eurasian cooling and Arctic warming. *Clim. Dyn.* **58**, 2725–2744 (2022).
68. Zhao, L. et al. The warm Arctic—cold Eurasia pattern and its key region in winter in CMIP6 model simulations. *Adv. Atmos. Sci.* **40**, 2138–2153 (2023).
69. Li, X. & Wang, S. Recent increase in the occurrence of snow droughts followed by extreme heatwaves in a warmer world. *Geophys. Res. Lett.* **49**, e2022GL099925 (2022).
70. Li, Y. et al. Local cooling and warming effects of forests based on satellite observations. *Nat. Commun.* **6**, 6603 (2015).
71. Lorenz, R., Jaeger, E. B. & Seneviratne, S. I. Persistence of heat waves and its link to soil moisture memory. *Geophys. Res. Lett.* **37**, <https://doi.org/10.1029/2010GL042764> (2010).
72. Wehrli, K., Guillod, B. P., Hauser, M., Leclair, M. & Seneviratne, S. I. Identifying key driving processes of major recent heat waves. *J. Geophys. Res. Atmos.* **124**, 11746–11765 (2019).
73. Holloway, J. E. et al. Impact of wildfire on permafrost landscapes: a review of recent advances and future prospects. *Permafr. Periglac. Process.* **31**, 371–382 (2020).
74. Intergovernmental Panel on Climate Change (IPCC). *The Ocean and Cryosphere in a Changing Climate*. (Cambridge University Press, 2022).

75. Zhao, L. et al. Permafrost changes and its effects on hydrological processes on Qinghai-Tibet Plateau. *Bull. Chin. Acad. Sci.* **34**, <https://doi.org/10.16418/j.issn.1000-3045.2019.11.006> (2019).
76. Zhang, R., Wang, H., Fu, Q., Rasch, P. J. & Wang, X. Unraveling driving forces explaining significant reduction in satellite-inferred Arctic surface albedo since the 1980s. *Proc. Natl Acad. Sci. USA* **116**, 23947–23953 (2019).
77. Hong, Y. et al. Arctic-associated increased fluctuations of midlatitude winter temperature in the 1.5° and 2.0° warmer world. *npj Clim. Atmos. Sci.* **6**, 26 (2023).
78. Overland, J. E. et al. Nonlinear response of mid-latitude weather to the changing Arctic. *Nat. Clim. Change* **6**, 992–999 (2016).
79. Guo, D., Li, D. & Hua, W. Quantifying air temperature evolution in the permafrost region from 1901 to 2014. *Int. J. Climatol.* **38**, 66–76 (2018).
80. Huang, J. et al. Recently amplified arctic warming has contributed to a continual global warming trend. *Nat. Clim. Change* **7**, 875–879 (2017).
81. Davy, R. & Griewank, P. Arctic amplification has already peaked. *Environ. Res. Lett.* **18**, 084003 (2023).
82. Dai, A., Luo, D., Song, M. & Liu, J. Arctic amplification is caused by sea-ice loss under increasing CO<sub>2</sub>. *Nat. Commun.* **10**, 121 (2019).
83. Vikhamar-Schuler, D. et al. Changes in winter warming events in the Nordic Arctic region. *J. Clim.* **29**, 6223–6244 (2016).
84. Sui, C., Zhang, Z., Yu, L., Li, Y. & Song, M. Investigation of Arctic air temperature extremes at north of 60°N in winter. *Acta Oceanol. Sin.* **36**, 51–60 (2017).
85. Ciavarella, A. et al. Prolonged Siberian heat of 2020 almost impossible without human influence. *Clim. Change* **166**, 9 (2021).
86. Salzano, R. et al. Detection of winter heat wave impact on surface runoff in a periglacial environment (Ny-Ålesund, Svalbard). *Remote Sens.* **15**, 4435 (2023).
87. Reyes, L. & Kramer, M. G. High-elevation snowpack loss during the 2021 Pacific Northwest heat dome amplified by successive spring heatwaves. *npj Clim. Atmos. Sci.* **6**, 208 (2023).
88. Copernicus Climate Change Services (C3S). *European State of the Climate 2019* (ECMWF, 2019).
89. Dunn, R. J. H. et al. Development of an updated global land in situ-based data set of temperature and precipitation extremes: HadEX3. *J. Geophys. Res. Atmos.* **125**, e2019JD032263 (2020).
90. Strand, S. M., Christiansen, H. H., Johansson, M., Åkerman, J. & Humlum, O. Active layer thickening and controls on interannual variability in the Nordic Arctic compared to the circum-Arctic. *Permafr. Periglac. Process.* **32**, 47–58 (2021).
91. Osterkamp, T. E. Characteristics of the recent warming of permafrost in Alaska. *J. Geophys. Res. Earth Surf.* **112**, <https://doi.org/10.1029/2006JF000578> (2007).
92. Smith, S. L., Throop, J. & Lewkowicz, A. G. Recent changes in climate and permafrost temperatures at forested and polar desert sites in northern Canada. *Can. J. Earth Sci.* **49**, 914–924 (2012).
93. Gottlieb, A. R. & Mankin, J. S. Evidence of human influence on Northern Hemisphere snow loss. *Nature* **625**, 293–300 (2024).
94. Pascual, D. & Johansson, M. Increasing impacts of extreme winter warming events on permafrost. *Weather Clim. Extrem.* **36**, 100450 (2022).
95. Liu, J., Xu, H., Tao, Y. & Lyu, Q. Effects of clay content and subfreezing temperature on the freeze–thaw deformation properties of clayey soils. *CATENA* **239**, 107916 (2024).
96. Hu, G. et al. Review of algorithms and parameterizations to determine unfrozen water content in frozen soil. *Geoderma* **368**, 114277 (2020).
97. Commane, R. et al. Carbon dioxide sources from Alaska driven by increasing early winter respiration from Arctic tundra. *Proc. Natl Acad. Sci. USA* **114**, 5361–5366 (2017).
98. Natali, S. M. et al. Large loss of CO<sub>2</sub> in winter observed across the northern permafrost region. *Nat. Clim. Change* **9**, 852–857 (2019).
99. Pedron, S. A. et al. More snow accelerates legacy carbon emissions from Arctic permafrost. *AGU Adv.* **4**, e2023AV000942 (2023).
100. Streletskiy, D. A., Shiklomanov, N. I. & Nelson, F. E. Permafrost, infrastructure, and climate change: a GIS-based landscape approach to geotechnical modeling. *Arct. Antarct. Alp. Res.* **44**, 368–380 (2012).
101. Rajendran, S. et al. Monitoring oil spill in Norilsk, Russia using satellite data. *Sci. Rep.* **11**, 3817 (2021).
102. Niu, F., Luo, J., Lin, Z., Fang, J. & Liu, M. Thaw-induced slope failures and stability analyses in permafrost regions of the Qinghai-Tibet Plateau, China. *Landslides* **13**, 55–65 (2016).
103. Polovtseva, M. A. Blessing and a Curse: Melting Permafrost in the Russian Arctic. <https://www.thearcticinstitute.org/blessing-curse-melting-permafrost-russian-arctic/> (2020).
104. Kuklina, V. et al. Fires on ice: emerging permafrost peatlands fire regimes in Russia's Subarctic Taiga. *Land* **11**, 322 (2022).
105. Zhang, Y. et al. The thermal response of permafrost to coastal floodplain flooding. *Environ. Res. Lett.* **18**, 035004 (2023).
106. Lewkowicz, A. G. & Way, R. G. Extremes of summer climate trigger thousands of thermokarst landslides in a High Arctic environment. *Nat. Commun.* **10**, 1329 (2019).
107. Ravanel, L., Magnin, F. & Deline, P. Impacts of the 2003 and 2015 summer heatwaves on permafrost-affected rock-walls in the Mont Blanc massif. *Sci. Total Environ.* **609**, 132–143 (2017).
108. Sheffield, J., Goteti, G. & Wood, E. F. Development of a 50-year high-resolution global dataset of meteorological forcings for land surface modeling. *J. Clim.* **19**, 3088–3111 (2006).
109. Thrasher, B. et al. NASA Global Daily Downscaled Projections, CMIP6. *Sci. Data* **9**, 262 (2022).
110. Karjalainen, O. et al. Circumpolar permafrost maps and geohazard indices for near-future infrastructure risk assessments. *Sci. Data* **6**, 190037 (2019).
111. Raei, E., Nikoo, M. R., AghaKouchak, A., Mazdiyasni, O. & Sadegh, M. GHWR, a multi-method global heatwave and warm-spell record and toolbox. *Sci. Data* **5**, 180206 (2018).

## Acknowledgements

This research was funded by the Second Tibetan Plateau Scientific Expedition and Research (STEP) program (grant No. 2019QZKK020108-1-02), the Special Program for Basic Investigation of S&T Resources of Ministry of Science and Technology, China (grant No. 2022FY100704), and the Startup Foundation for Introducing Talent of NUIST (grant No. 2024r084).

## Author contributions

X.L. and L.Z. designed the research. X.L. and X.C. performed the research and wrote the manuscript. S.W. and L.W. contributed new analytic tools and ideas. All the co-authors revised the manuscript.

## Competing interests

The authors declare no competing interests.

## Additional information

**Supplementary information** The online version contains supplementary material available at <https://doi.org/10.1038/s41612-025-01037-5>.

**Correspondence** and requests for materials should be addressed to Lin Zhao.

**Reprints and permissions information** is available at <http://www.nature.com/reprints>

**Publisher's note** Springer Nature remains neutral with regard to jurisdictional claims in published maps and institutional affiliations.

**Open Access** This article is licensed under a Creative Commons Attribution-NonCommercial-NoDerivatives 4.0 International License, which permits any non-commercial use, sharing, distribution and reproduction in any medium or format, as long as you give appropriate credit to the original author(s) and the source, provide a link to the Creative Commons licence, and indicate if you modified the licensed material. You do not have permission under this licence to share adapted material derived from this article or parts of it. The images or other third party material in this article are included in the article's Creative Commons licence, unless indicated otherwise in a credit line to the material. If material is not included in the article's Creative Commons licence and your intended use is not permitted by statutory regulation or exceeds the permitted use, you will need to obtain permission directly from the copyright holder. To view a copy of this licence, visit <http://creativecommons.org/licenses/by-nc-nd/4.0/>.

© The Author(s) 2025